Planetary Imaging Concept Testbed Using a Recoverable Experiment–Coronagraph (PICTURE C)

Timothy Cook
Kerri Cahoy
Supriya Chakrabarti
Ewan Douglas
Susanna C. Finn
Marc Kuchner
Nikole Lewis
Anne Marinan
Jason Martel
Dimitri Mawet
Benjamin Mazin
Seth R. Meeker
Christopher Mendillo
Gene Serabyn

SPIE.

Planetary Imaging Concept Testbed Using a Recoverable Experiment–Coronagraph (PICTURE C)

Timothy Cook,[a,*] **Kerri Cahoy,**[b] **Supriya Chakrabarti,**[a] **Ewan Douglas,**[c] **Susanna C. Finn,**[a] **Marc Kuchner,**[d]
Nikole Lewis,[e] **Anne Marinan,**[b] **Jason Martel,**[a] **Dimitri Mawet,**[f] **Benjamin Mazin,**[g] **Seth R. Meeker,**[g]
Christopher Mendillo,[a] **Gene Serabyn,**[h] **David Stuchlik,**[i] **and Mark Swain**[h]
[a]University of Massachusetts–Lowell, 600 Suffolk Street, Lowell, Massachusetts 01854, United States
[b]MIT, 77 Massachusetts Avenue, Building 33, Cambridge, Massachusetts 02139-4301, United States
[c]Boston University, 725 Commonwealth Avenue, Boston, Massachusetts 02215, United States
[d]NASA Goddard Space Flight Center, NASA GSFC, Code 667, Greenbelt, Maryland 20771, United States
[e]Space Telescope Science Institute, 3700 San Martin Drive, Baltimore, Maryland 21218, United States
[f]Caltech, Astronomy Department, MC 249-17 1200 E. California Boulevard, Pasadena, California 91125, United States
[g]University of California, Department of Physics, Santa Barbara, California 93106, United States
[h]Jet Propulsion Laboratory, 4800 Oak Grove Drive, Pasadena, California 91109-8001, United States
[i]NASA, Wallops Flight Facility, Code 820 Building E 107, Wallops Island, Virginia 23337, United States

Abstract. An exoplanet mission based on a high-altitude balloon is a next logical step in humanity's quest to explore Earthlike planets in Earthlike orbits orbiting Sunlike stars. The mission described here is capable of spectrally imaging debris disks and exozodiacal light around a number of stars spanning a range of infrared excesses, stellar types, and ages. The mission is designed to characterize the background near those stars, to study the disks themselves, and to look for planets in those systems. The background light scattered and emitted from the disk is a key uncertainty in the mission design of any exoplanet direct imaging mission, thus, its characterization is critically important for future imaging of exoplanets. © *The Authors. Published by SPIE under a Creative Commons Attribution 3.0 Unported License. Distribution or reproduction of this work in whole or in part requires full attribution of the original publication, including its DOI.* [DOI: 10.1117/1.JATIS.1.4.044001]

1 Introduction

The study of exoplanets is one of the most exciting astronomical endeavors of our time. It engages us at the philosophical, scientific, and practical levels. Philosophically, it goes to the heart of some of our deepest questions about what it means to be human. Are we alone in the Universe? Is Earth unique? Where is everybody? Scientifically, it probes fundamental astrophysical questions about the origin of stellar systems, the mechanics of disks, and the physics of planetary surfaces and atmospheres. At a practical level, it provides a unique laboratory to test the models of planetary atmospheres (including Earth) and the underlying physics built into those models under a wider variety of parameters and conditions than is possible observing solar system objects alone.

As a field, exoscience has made astonishing progress. In 1990, we knew of no planets beyond Pluto. In 1992, the first confirmed exoplanet was discovered.[1] Other discoveries quickly followed: the first exoplanet orbiting a main sequence star,[2] the first transiting system,[3] and the first direct image of a planetary-mass companion.[4] The catalog of known exoplanets has grown to over 1800 planets in over 1100 star systems and over 50 directly imaged planetary-mass objects have been cataloged[5]—mostly young, and therefore hot, systems observed in the infrared (IR).

As the discovery of exoplanets becomes routine, we are beginning to move from cataloging planets and measuring occurrence statistics to studying each in detail. In order to do so, we need to collect light from the planet, not just indirectly infer its properties from its effect on the appearance of its host star. While work can be, and has been, done using the differential brightness of the system through a planet's orbital phase and across transits,[6,7] detailed study of a large number of planets will be better enabled by direct imaging of those planets.

The direct imaging of exoplanets in both IR and visible light is inescapably convolved with the direct imaging of exozodiacal dust. Dust pervades planetary systems. Direct thermal emission from dust in the IR and starlight reflected by dust in the visible are the dominant astrophysical backgrounds against which exoplanets will be imaged. Furthermore, structures such as rings and clumps that form in exozodiacal clouds can both confound and benefit exoplanet observations. Dust grains in the mean motion resonances of Earth-massed exoplanets may form rings that are brighter than the planets themselves.[8] Observations of these structures could enable the indirect discovery of planets. Conversely, compact dust structures can mimic the appearance of planets in low-resolution images, confusing possible detections.

Several direct imaging balloon mission concepts have been explored over the past decade. Predicting that telescopes up to 10 m in diameter will achieve their diffraction limit at balloon altitudes, Ford et al.[9] first discussed the performance of a long-duration stratospheric exoplanet imaging mission using

*Address all correspondence to: Timothy Cook, E-mail: Timothy_Cook@uml.edu

a coronagraphic stop and a Hubble class telescope. Traub et al.[10] explored atmospheric scintillation effects from a balloon-born laser interferometer and extrapolated that a stratospheric exoplanet imager could achieve 10^{-9} contrast at 0.5″ without requiring active wavefront control. The Wallops Pointing system[11] has been used as the baseline for several larger mission concepts. Bryden et al.[12] and Roberts et al.[13] explored long-duration flights with four channel imaging coupled to 1.1 and 0.75 m telescopes, respectively, and found that tens of debris disks are within range of such missions. Meanwhile, imaging and coronagraph technology has developed to allow more compact and lightweight high-contrast balloon payloads.

This paper describes one such mission, the Planetary Imaging Concept Testbed Using a Recoverable Experiment–Coronagraph (PICTURE C). It is funded to fly on a conventional (as opposed to long-duration) high-altitude balloon—the Astrophysics Research and Analysis suborbital program. PICTURE C will image disks of nearby systems in ≲10 AU in scattered visible light. It will also be able to detect any planets with contrasts brighter than $1:10^7$ present in those systems.

PICTURE C is the next in a series of experiments that began with the PICTURE sounding rocket mission.[14] PICTURE used a visible nulling coronagraph (VNC) in conjunction with a 0.5 m on-axis Gregorian telescope in order to image the dust environment in the inner system of ϵ; Eri. The mission was launched on October 8, 2011, from White Sands Missile Range, but suffered a failure of the science data telemetry channel 80 s into flight. The flight did produce housekeeping data that was used to verify the pointing system performance.[15] The flight also demonstrated that the coronagraph and cameras survived the flight, but could not verify the system's in-flight nulling performance. In order to complete the demonstration of the VNC intended for the PICTURE effort, we are currently preparing the PICTURE system for flight as PICTURE B. That sounding rocket flight is scheduled for the fall of 2015.[16,17]

2 Goals and Constraints

While the specifics of the implementation of a large exoplanetary imaging mission are debated,[18–20] the overall mission requirements are well understood. It must be able to detect Earthlike planets in one year orbits around Sunlike stars. Visible and IR systems both probe interesting, but different, physical regimes, and both will be required for a comprehensive study of extrasolar systems.

Because of the requirements of adaptive optics systems, ground-based exoplanet coronagraphs will be limited to IR observations for the foreseeable future. In order to measure the visible light scattered by exoplanets, it will be necessary to make measurements from above the atmosphere with either a stratospheric or space system. Visible measurements are necessary because they probe different physical properties of the planets than the IR measurements. Infrared, ground-based, measurements will record blackbody continuum and molecular line emission while visible light coronagraphs will be sensitive to haze and clouds as well as key trends, such as Rayleigh scattering slopes. Space-based visible light coronagraphs will be sensitive to atmospheric structure and albedo, while IR experiments will be sensitive to composition and temperature. Since hazes in the atmosphere present a significant complication to the interpretation of IR spectra,[21] the combination of visible and IR measurements will be more powerful than either alone.

Table 1 Key design parameters.

Primary diameter	60 cm
Central wavelength	600 nm
Bandpass	20%
Inner working angle (IWA)	$1.5\lambda_{max}/D$
IWA	0.34″
IWA	1 AU @ 3 pc
Contrast at IWA	10^7
Resolving power ($\lambda/\Delta\lambda$)	20
Total observing time	~8.4 h

In order to prepare for these large future missions, we need to begin to fly more modest systems at lower cost to prove systems and methods and to gain experience with real-world data sets. The key parameters for an exoplanet coronagraph are the maximum contrast it can measure (ratio of host star to planet flux) and the minimum angle from the star at which it can achieve this contrast [the inner working angle (IWA)].

As a first step in detecting planets in Earthlike orbits, we must understand the dust and debris disks in the inner region of nearby systems. To image those disks, our instrument must have a suitable IWA and enough contrast to image the disk. There are only 7 star systems within 3 pc of the Sun, but over 40 within 5 pc. Thus, the system needs an IWA small enough to measure the inner system of stars out to 3 to 5 pc and must have sufficient contrast to measure the disk. At the same time, the system should be able to detect at least some planets. At a minimum, it should be able to detect Jovian planets in systems within 5 pc.

These considerations led us to design PICTURE C with the performance listed in Table 1.

The performance of the PICTURE C system is further constrained by the observing opportunities of the balloon platform. The balloon flights are launched from eastern New Mexico, and because of the atmospheric conditions in the stratosphere, they must fly in the spring and fall. Because of programmatic considerations, most fly in the fall. The flights typically can span a full night but are unlikely to span two. This fixes both the region of the sky that is available and the total observing time. An observing program of three targets per flight with 2 h time-on-target each has been selected as the best compromise among the number of targets, signal to noise on each target, and adequate calibration and pointing overhead. Furthermore, targets must span the sky so that successive targets are available throughout the night. ϵ Eri, α Aql, and τ Cet have been selected as the strawman target list.

3 Instrument

The PICTURE C instrument is an off-axis afocal Gregorian telescope with the coronagraph mounted behind the primary mirror. The telescope is mounted on the Wallops ArcSecond Pointing (WASP) system, a balloon gondola with gimbal to point the telescope to ~1″ in pitch and yaw (see Fig. 1). The roll around the pointing axis is not controlled. The system has several active elements to further stabilize the pointing and to correct
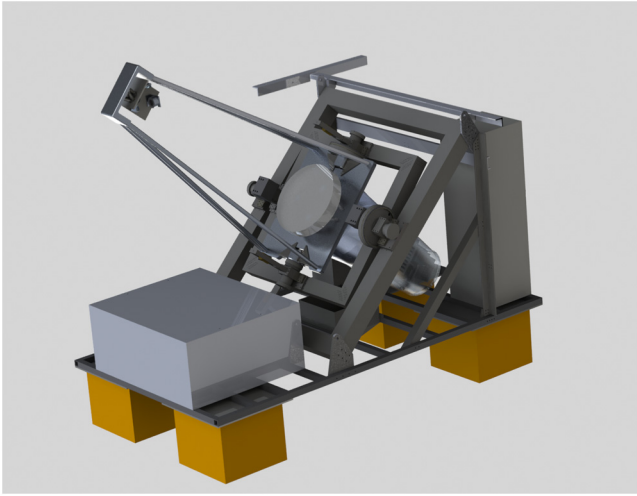
Fig. 1 PICTURE C uses a 60 cm clear aperture, off-axis, Gregorian telescope in the Wallops ArcSecond Pointing (WASP) system. The clear aperture system allows PICTURE C to implement a high-performance vector vortex coronagraph while the use of the WASP system provides high pointing precision at low cost.

for thermal, mechanical, and optical distortions. Low-order wavefront correction (LOWC) is provided by an active hexapod secondary mount that can adjust the secondary position and orientation and a high-speed integrated wavefront controller (IWC), which are described in more detail in Sec. 3.2.2.

Because the roll orientation of the telescope is not controlled, the image of the sky will rotate on the detector. This will result from both the motion of the payload as the gondola swings under the balloon (∼0.5 deg) and the rotation of the sky through the night. PICTURE C uses a photon counting microwave kinetic inductance detector (MKID), which will allow us to record the position and energy of any detected photon, as well as its arrival time. The time information will allow us to derotate images and to eliminate the associated blurring (see Sec. 3.1.1). The sky rotation will be used to differentiate true sources on the sky from speckles arising in the optical system.[22,23]

3.1 Mechanical Design

The mechanical design for PICTURE C is fairly conventional. The telescope occupies a cylindrical volume with the secondary mirror on the side of the cylinder. Since we are using a Gregorian secondary, we can position a field stop at the prime focus to reject stray light. A video camera will be focused on the outside of this aperture to assist in target acquisition. Outward from the prime focus is an assembly containing the secondary mirror, the IWC, and fold mirrors to direct the beam back to the instrument. The assembly is held on a six axis positioning hexapod to allow adjustments to the collimation and focus as the structure moves thermally and mechanically in flight.

The instrument will be mounted behind the primary mirror as if the telescope were a conventional on-axis telescope. Fold mirrors will bring the beam, which passes from the secondary subassembly past the side of the primary, radially inward across the back of the primary mirror. The light will be directed along the central axis of the tube into the instrument. This allows us to hold the center of mass of the total package behind the primary mirror and at the center of rotation of the WASP gimbal.

3.1.1 WASP pointing system

PICTURE C is enabled by the WASP system. We plan to use the two-axis WASP system (pitch and yaw), which has been demonstrated in flight to ≲1 arcsec.[11] The PICTURE C design does not include the three-axis WASP system (roll, pitch, and yaw), which would reduce the detector requirements, but includes some additional risk as that system is still in development. We have conducted a detailed simulation[15] to assess the combined performance of the WASP system with the PICTURE C LOWC system. The result of those simulations is shown in Fig. 3.

Because we are using the two-axis WASP design, the pendulum motion of the gondola under the balloon will cause the sky to appear to rotate. A nominal swing of 0.5 deg corresponds to 0.5 pixels at the edge of the field of view. By using the high time resolution capability of an MKID (see Sec. 3.3) and the attitude knowledge provided by the WASP system, we are able to derotate the image as it is recorded.

3.1.2 Thermal design

Temperatures at balloon float altitudes (∼35 to 45 km) are typically near −40°C. To operate at that temperature, and to hold alignment through the temperature change from the alignment laboratory to the observing environment, the PICTURE C design includes a low-order wavefront control system (see Sec. 3.2.2) to compensate for any changes in the optical system. In order for those active components, as well as the other electronics, to operate properly, a number of heaters will maintain their operating temperature near 20°C.

The heaters will create some level of dome seeing, but given the low ambient pressure, it is thought to be insignificant. While it is difficult to make precise predictions of the effects of this turbulence, we can put some order of magnitude bounds on the effect. The pressure at float altitude is ∼2.5 torr—or 0.4% of the sea level density if the temperature change is also considered. The index of refraction (n) of air at standard temperature and pressure is about $n - 1 = 3 \times 10^{-4}$. The index of refraction varies linearly with density (ρ),[25] so the index at float altitude is approximately $n - 1 = 1 \times 10^{-6}$. The largest length scale is the size of the instrument, ∼2 m. The difference between the optical path length through a 2 m instrument with stratospheric air and the path length through the instrument with vacuum is 2 microns. Any density changes due to turbulence will affect that 2 micron path length difference. In order to operate properly, we can accept a phase change of no more than <0.5 nm due to air turbulence (corresponding to ∼$\lambda/1000$); this implies $(n - 1)/\Delta(n - 1) > 4000$. In order to assess how reasonable this specification is we note that this level of turbulence corresponds to pressure waves of 25 Pascals at sea level or roughly the equivalent to the sound waves from a trumpet at 0.5 m and conclude that dome seeing will not limit our performance.

3.2 Optical Design

The PICTURE C optical system consists of a telescope, a low-order wavefront corrector (LOWC), and a vector vortex coronagraph (VVC). The telescope primary will be polished to $\lambda/10$, and all other optics will be polished to $\lambda/20$. Both of these tolerances are well within the state of the art for mirrors of their respective sizes.

The telescope is an off-axis, clear aperture, configuration. The unobscured aperture avoids diffraction effects from the

Table 2 System throughput.

Primary diameter	60 cm
Geometric area	2827 cm^2
Lyot stop diameter	90%
Lyot stop area	81%
Number of reflections	9
Reflection efficiency	97%
Detector quantum efficiency	40%
Throughput	24.6%
Eff. area	696 cm^2

spider and secondary and is required by the VVC. Because the PICTURE C telescope has no central obscuration, the 0.6 m balloon telescope delivers a significantly larger collecting area than the 0.5 m on-axis telescope with the central obscuration used in earlier PICTURE flights.

We have elected to use a Gregorian design rather that the more common Cassegrain because it forms a real exit pupil

(rather than the virtual one formed by the Cassegrain). The LOWC actuator, which consists of a combined tip-tilt-piston actuator and a 76 actuator deformable mirror (DM) in a single unit called an IWC, is placed in this pupil plane. As a result, the beam will only walk on a single optic (the secondary) as the steering mirror stabilizes the beam. Thus, the contrast-limiting effects of beam walk will be minimized.

Estimates of the system throughput are given in Table 2, and a diagram of the optical system is given in Fig. 2.

3.2.1 Telescope

The PICTURE C telescope is a 60 cm off-axis afocal Gregorian system. The secondary, a simple off-axis parabola, will be mounted on a six degrees of freedom hexapod for ease of alignment and to correct for strains in the optical bench during flight. Our trade studies indicate that a 60 cm clear aperture telescope is the best compromise between cost and performance. It is small enough to be fabricated at low cost while being large enough to meet our scientific goals. We have elected to use an off-axis, unobstructed aperture because it enables a simpler, lower-risk coronagraph design. While a larger telescope would enable more and more precise observations, the added costs are significant. In addition, the larger system puts larger burdens on the
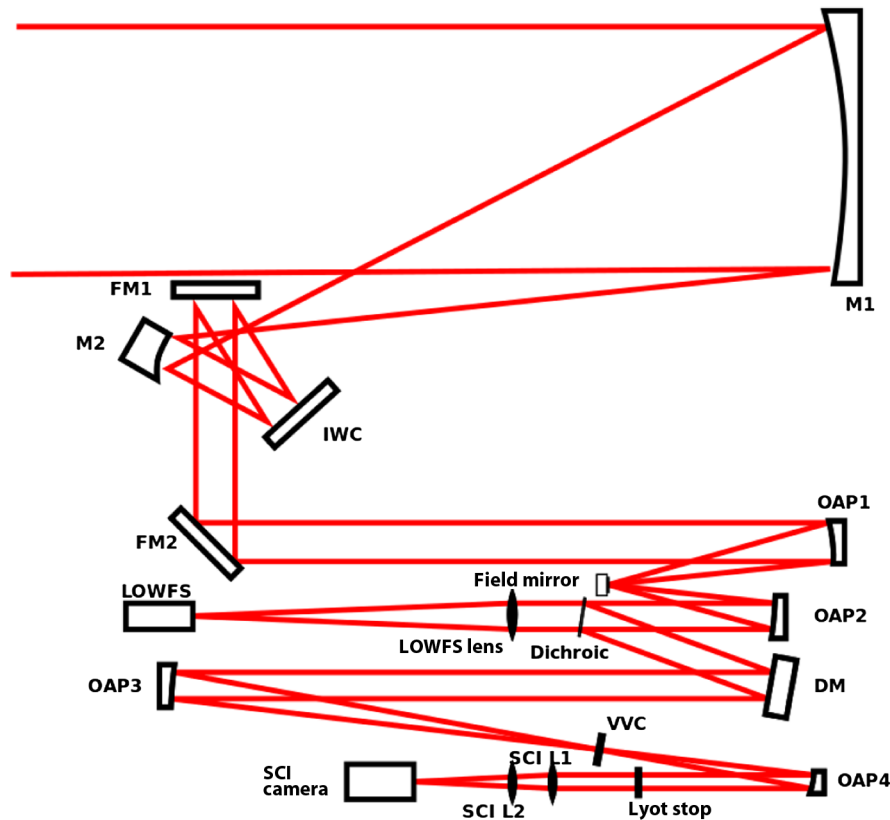

Fig. 2 The design of the PICTURE C coronagraph follows that of Mawet.[26] The system uses an $f/2.5$ primary (M1). An afocal, off-axis, Gregorian secondary (M2), two fold mirrors (FM1 and FM2), and an integral wavefront controller (IWC; see Sec. 3.2) are mounted at the telescope exit pupil using a hexapod mount so that the secondary can be realigned in flight (see Sec. 3.1). From there, the beam is compressed (OAP1, OAP2, and the field mirror) and light for the low order wave front sensor (LOWFS) is picked off using a dichroic beam splitter. The heart of the system is a high-order deformable mirror (DM) to control higher-order aberration (see Sec. 3.2.3) and a vector vortex coronagraph (OAP3, VVC, and OAP4) in the Mawet[26] configuration with a Lyot stop and camera lenses (SCI L1 and SCI L2) to form the image. The data are recorded using a microwave kinetic inductance detector (SCI camera, see Sec. 3.3).
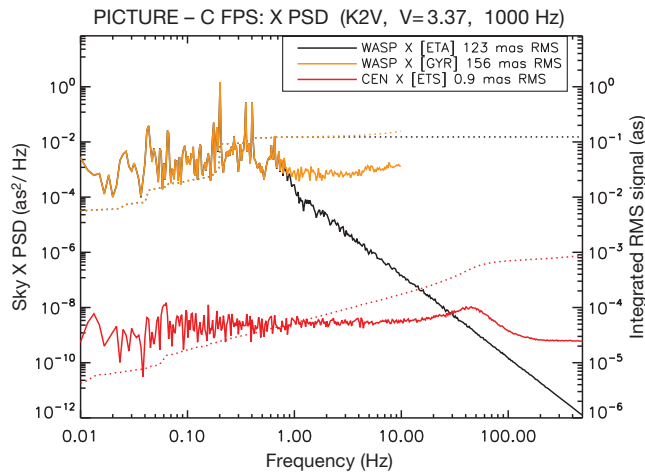
Fig. 3 The best measured power spectrum of the WASP (orange line[24]) is limited by the sensor noise floor at all frequencies above ~1 Hz. In order to estimate our pointing performance (red line), we have assumed a high-frequency roll off similar to that seen in PICTURE (black line).[15] This is physically reasonable based on the payload's moments of inertia. The solid lines present the power spectral density, while the dashed lines are the cumulative pointing error and, thus, represent the total disturbance.

mechanical system, the pointing system, etc. This cascades to more expensive structures, pointing systems, etc.

3.2.2 Low-order wavefront correction system

In order to maintain the high Strehl ratio required, PICTURE C will use two active elements to correct the low-order wavefront errors.

PICTURE C will use a six degrees of freedom secondary mount to recollimate and focus the telescope as thermal expansion distorts the optical bench. The mount is designed to remove gross misalignments caused by thermal stresses and/or launch loads and, thus will operate infrequently.

More active control will be achieved by a combination of a tip-tilt actuator and a coarse DM—a Xinetics IWC,[27] located at the pupil created by the Gregorian secondary. This system will be used to correct distortions left after repositioning the secondary or caused by changing mechanical stress as the gondola swings under the balloon. Our simulations (see Fig. 3) indicate that the IWC will provide 1 mas pointing stabilization at 1 kHz. This pointing system is directly adapted from the PICTURE B system that has demonstrated 5 mas stability on the PICTURE sounding rocket flight.[15]

3.2.3 High-order wavefront control system

PICTURE C, like all internal coronagraphs, requires a DM to correct high-order wavefront errors. We have elected to use the Xinetics 32×32 actuator PHO1S1-1024 deformable mirror. The choice was driven by cost, surface quality, actuator count, and the probability of having a nonresponsive actuator in the field of view.

We considered two methods to control that DM: electric field conjugation (EFC),[28] similar to that used in the JPL High Contrast Imaging Testbed (HCIT) or PALM-3000,[29] and interferometric phase mapping, similar to that used on GPI and PICTURE B. We have elected to use EFC as this method is well explored in the literature[30–32] and requires no additional

hardware. As described in those works, EFC does require a pre-flight model and calibration to establish the DM influence function. A significant task through development will be to assess the efficacy of this technique on the as built hardware.

3.2.4 Coronagraph

PICTURE C will use a VVC. While other methods (nullers,[33,34] pupil plane coronagraphs,[35] other image plane coronagraphs,[36] and hybrid pupil plane/image plane systems[37]) all have strengths, we selected the VVC because it is optically simple, has been field tested,[38] and has a high performance.[26] We plan to use a one inch filter from Beam Co. fabricated using the same liquid crystal techniques as those used in the previous works. The VVC intrinsically operates in unpolarized light,[39] but polarizers are frequently used to improve performance as the aberrations of each polarization are subtly different. We plan to use the coronagraph without the polarizing filters envisioned in higher performing systems. While using the VVC in unpolarized light will limit the performance to contrasts of $10^8 : 1$, this should be sufficient to meet the PICTURE C goals.

3.3 Detector

MKIDs[40] have several properties that make them attractive for the PICTURE C experiment. They are time tagged, photon counting detectors, have intrinsic energy resolution, and operate with very low noise levels. By photon counting, they operate without any read noise and can thus operate with high time resolution without any associated read noise penalty. As a photon counting detector, MKID records a single word for each photon it records. This 64-bit word encodes the pixel in which the photon was detected, the energy of the photon, and its arrival time. As a result, the data rate and resultant data storage required are proportional to the count rate on the detector. If the coronagraph is successfully blocking the starlight, we expect count rates of several 100 photons/s over the full detector with resulting data sizes of a few hundred megabytes of data. However, during acquisition and as the active components are adjusted, we will see much higher count rates and will size the data system accordingly.

Because PICTURE C has baselined the two-axis WASP system, the field of view will appear to rotate slightly back and forth on the focal plane as the payload swings under the balloon. Any CCD-based system will need a reasonably slow read out in order to minimize read noise. As a result, the image may be slightly blurred in the azimuthal direction (about the central star). The high time resolution of the MKID will allow us to correct this rotation and to increase our spatial resolution in an effort to detect both ϵ Eri b and any heretofore undiscovered planets that may be in any of the systems observed.

The cryogenics for the MKID camera are expected to be a duplicate of the existing cryostat for the DARKNESS project at Palomar. This system consists of an LN_2 and LHe shielded dewar with over 24 h of hold time. A high-precision device adiabatic demagnetization refrigerator (ADR) is located at the 4.2 K stage of this cryostat. The ADR cools the MKID array from 4.2 K to 100 mK with a hold time goal of 24 h.

Optical access to the device is provided by a series of flat antireflection coated windows in the cryostat at 300 K, 77 K, 4.2 K, and 100 mK. The 4.2 K window is coated with a multi-layer bandpass filter to pass the optical band but reject the near-IR. The 100 mK filter is coated with indium tin oxide to reflect
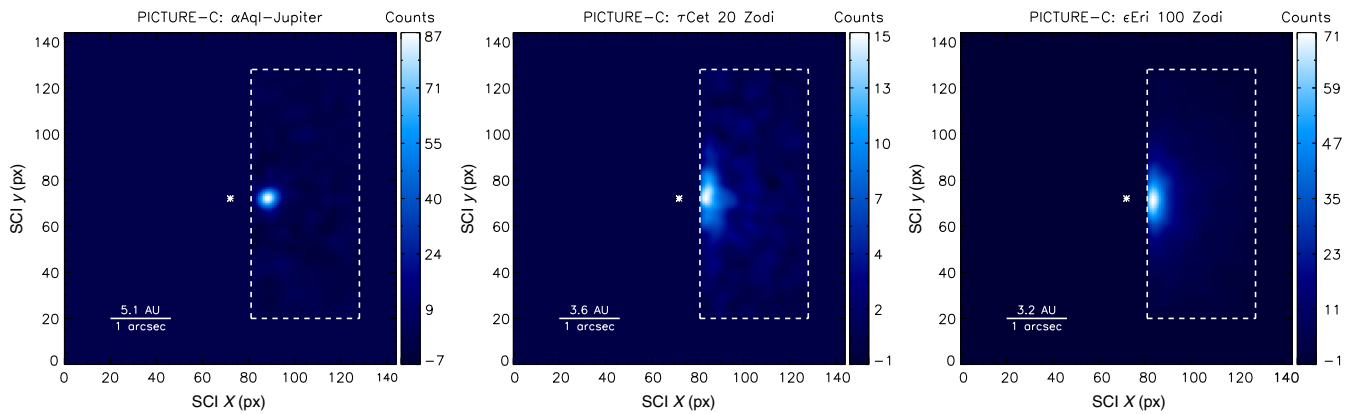
Fig. 4 These simulations, made using Zodiacal Cloud Image Synthesis,[42] show the PICTURE C capabilities. We have simulated a $1R_j$ planet around α Aql, a small (20 zodi) dust disk around τ Cet, and a large one (100 zodi) around ϵ; Eri. These simulations are not meant to show an actual planet or dust distribution but rather to highlight our capabilities. The instrument can detect $\lesssim$10 zodi disks or Jovian planets around nearby stars. These simulations use VVC performance data from the high-contrast imaging testbed[43] to estimate speckle patterns, contrast, and inner working angle.

long-wavelength IR. This filter arrangement has proven sufficient in the ARCONS instrument.

4 Model Results

We have simulated the performance of the PICTURE C system with a model that uses basic parameters, such as observing time, effective area, and expected contrast. The observing time is derived from the PICTURE C observing plan, while the effective area comes from the detailed instrument design. The contrast map assumed is modeled after a measurement made using a VVC at the JPL HCIT. While conditions in flight will undoubtedly be different from that in the HCIT, this represents our best estimate of the actual performance. Based on our nominal observing plan, we assume a total exposure time per target of 2 h.

The model begins by building an image of the target star. We use a Kurucz model atmosphere (based on the star's spectral type) to predict the stellar spectrum.[41] This is combined with the expected effective area to get the expected count rate and, hence, the total integrated point spread function (PSF), which, given the predicted high Strehl ratios of the PICTURE C system, is assumed to be an Airy spot.

To find the expected dust flux, we use Zodiacal Cloud Image Synthesis[42] to produce a 1 zodi cloud around the target star. We convert that to a pixel-by-pixel count rate and scale by the total observing time. This is further scaled to get images of $1, 5, \ldots,$ zodis.

The stellar leakage (i.e., unmasked star light) is added by assuming that leakage contributes light across the image in the PICTURE C coronagraph in the same manner it does for the VVC in HCIT laboratory measurements. We scale the leakage model to the estimated stellar flux and add additional background to account for a low-level uniform background of diffuse light and scattering.

If the particular simulation includes a known planet, we use the planet parameters from the Extrasolar Planets Encyclopaedia.[5] In the case of stars with no known planet, we have assumed a Jupiter sized planet $3\lambda/D$ from the host star. The reflected signal from the planet is based on the planet-star separation,

the star's brightness, and the planet's albedo, which is assumed to be similar to Jupiter's geometric albedo of ~0.5.

Once all of these signal and background terms have been accumulated, Poisson noise is generated based on the expected total counts/pixel. MKIDs are photon counting devices and are, thus, free from read noise. Furthermore, properly tuned MKIDs have high enough sensitivity that all photons in our bandpass have energies that are far above the threshold set by the readout phase noise; we do not suffer from any dark counts.

The resulting noisy images are then treated in the same manner as we will treat the flight images. (In practice, we will test a variety of analysis methods on the real data.) We assume that the system PSF is well characterized. A model calibration PSF is used to background subtract the flight image, leaving speckles consistent with the photon noise limit. The procedure necessarily misses PSF calibration errors, but captures all random (Poisson) noise and accurately simulates the image flat fielding process. The resulting background subtracted image is then smoothed with a kernel appropriate to the PSF. The results are presented in Fig. 4.

5 Summary

PICTURE C will spectrally image debris disks and possibly exojupiters that are undetectable by radial velocity and transit methods. The data will allow us both to better understand those disks and to quantify the effect of exozodiacal light on other exoplanet observations. In addition to detecting disks, it will be sensitive to exojupiters between 0.34 and 2.29" from their parent star. It achieves these results with a modest aperture telescope, field proven subsystems, and flight tested pointing systems. The conservative design allows this project to be flown on a conventional balloon in order to return results in the near future.

References

1. A. Wolszczan and D. A. Frail, "A planetary system around the millisecond pulsar PSR1257 + 12," *Nature* **355**, 145–147 (1992).
2. M. Mayor and D. Queloz, "A Jupiter-mass companion to a solar-type star," *Nature* **378**, 355–359 (1995).
3. D. Charbonneau et al., "Detection of planetary transits across a Sun-like star," *Astrophys. J.* **529**, L45–L48 (2000).
4. G. Chauvin et al., "A giant planet candidate near a young brown dwarf. Direct VLT/NACO observations using IR wavefront sensing," *Astron. Astrophys.* **425**, L29–L32 (2004).
5. J. Schneider et al., "Defining and cataloging exoplanets: the exoplanet.eu database," *Astron. Astrophys.* **532**, A79 (2011).
6. J. J. Fortney et al., "Transmission spectra of three-dimensional hot Jupiter model atmospheres," *Astrophys. J.* **709**, 1396–1406 (2010).
7. R. T. Zellem et al., "The 4.5 μm full-orbit phase curve of the hot Jupiter HD 209458b," *Astrophys. J.* **790**, 53 (2014).
8. C. C. Stark and M. J. Kuchner, "The detectability of exo-Earths and super-Earths via resonant signatures in exozodiacal clouds," *Astrophys. J.* **686**, 637–648 (2008).
9. H. C. Ford et al., "Artemis: a stratospheric planet finder," *Adv. Space Res.* **30**, 1283–1288 (2002).
10. W. A. Traub et al., "Planetscope: an exoplanet coronagraph on a balloon platform," *Proc. SPIE* **7010**, 70103S (2008).
11. D. Stuchlik and J. Lanzi, "Wallops Arc-Second Pointer (WASP) test flight two data report," (2012).
12. G. Bryden et al., "Zodiac II: debris disk science from a balloon," *Proc. SPIE* **8151**, 81511E (2011).
13. L. C. Roberts et al., "The Debris Disk Explorer: a balloon-borne coronagraph for observing debris disks," *Proc. SPIE* **8864**, 88640A (2013).
14. S. R. Rao et al., "Path length control in a nulling coronagraph with a MEMS deformable mirror and a calibration interferometer," *Proc. SPIE* **6888**, 68880B (2008).
15. C. B. Mendillo et al., "Flight demonstration of a milliarcsecond pointing system for direct exoplanet imaging," *Appl. Opt.* **51**, 7069 (2012).
16. C. B. Mendillo et al., "PICTURE: a sounding rocket experiment for direct imaging of an extrasolar planetary environment," *Proc. SPIE* **8442**, 84420E (2012).
17. E. S. Douglas et al., "Status of the PICTURE sounding rocket to image the Epsilon Eridani circumstellar environment," in *American Astronomical Society Meeting Abstracts*, p. 122, American Astronomical Society (2014).
18. S. Seager et al., *Exo-S: Starshade Probe-Class Exoplanet Direct Imaging Mission Concept*, CreateSpace Independent Publishing Platform, http://exep.jpl.nasa.gov/stdt/Exo-S_Starshade_Probe_Class_Final_Report_150312_URS250118.pdf (2015).
19. K. Stapelfeldt et al., "EXO-C: imaging nearby worlds," Technical Report, http://exep.jpl.nasa.gov/stdt/Exo-C_Final_Report_for_Unlimited_Release_150323.pdf (2015).
20. D. Spergel et al., "Wide-Field InfraRed Survey Telescope-astrophysics focused telescope assets WFIRST-AFTA final report," 23 May 2013, http://wfirst.gsfc.nasa.gov/science/sdt_public/WFIRST-AFTA_SDT_Final_Report_Rev2_130524.pdf (15 August 2015).
21. K. B. Stevenson et al., "Transmission spectroscopy of the hot Jupiter WASP-12b from 0.7 to 5 μm," *Astron. J.* **147**, 161 (2014).
22. C. Marois et al., "Angular differential imaging: a powerful high-contrast imaging technique," *Astrophys. J.* **641**, 556–564 (2006).
23. D. Lafrenière et al., "A new algorithm for point-spread function subtraction in high-contrast imaging: a demonstration with angular differential imaging," *Astrophys. J.* **660**, 770–780 (2007).
24. J. Lanzi, private communication, NASA GSFC/WFF, Code 598, Wallops Island.
25. P. E. Ciddor, "Refractive index of air: new equations for the visible and near infrared," *Appl. Opt.* **35**, 1566 (1996).
26. D. Mawet et al., "Recent results of the second generation of vector vortex coronagraphs on the high-contrast imaging testbed at JPL," *Proc. SPIE* **8151**, 81511D (2011).
27. B. W. Frazier et al., "Design and operation of an integrated wavefront corrector (IWC)," *Proc. SPIE* **5169**, 90–94 (2003).
28. A. Give'on et al., "Broadband wavefront correction algorithm for high-contrast imaging systems," *Proc. SPIE* **6691**, 66910A (2007).
29. R. Dekany et al., "PALM-3000: exoplanet adaptive optics for the 5 m Hale telescope," *Astrophys. J.* **776**, 130 (2013).
30. E. Cady et al., "Electric field conjugation with the project 1640 coronagraph," *Proc. SPIE* **8864**, 88640K (2013).
31. E. Sidick et al., "Studies of the effects of optical system errors on the HCIT contrast performance," *Proc. SPIE* **8151**, 815106 (2011).
32. J. E. Krist, S. B. Shaklan, and M. B. Levine, "Extraction of extrasolar planet spectra from realistically simulated wavefront-corrected coronagraphic fields," *Proc. SPIE* **7010**, 701044 (2008).
33. B. M. Levine et al., "The visible nulling coronagraph: architecture definition and technology development status," *Proc. SPIE* **6265**, 62651A (2006).
34. B. Hicks et al., "Monolithic achromatic nulling interference coronagraph: design and performance," *Appl. Opt.* **48**, 4963–4977 (2009).
35. N. J. Kasdin et al., "Optimal one-dimensional apodizations and shaped pupils for planet finding coronagraphy," *Appl. Opt.* **44**(7), 1117–1128 (2005).
36. M. J. Kuchner and W. A. Traub, "A coronagraph with a band-limited mask for finding terrestrial planets," *Astrophys. J.* **570**, 900–908 (2002).
37. A. Carlotti, D. Mawet, and L. Pueyo, "Optimal apodizers for the vector vortex coronagraph with on-axis telescopes," *Proc. SPIE* **8864**, 88641P (2013).
38. D. Mawet et al., "A dim candidate companion to epsilon Cephei," *Astrophys. J.* **738**, L12 (2011).
39. D. Mawet et al., "Optical vectorial vortex coronagraphs using liquid crystal polymers: theory, manufacturing and laboratory demonstration," *Opt. Express* **17**, 1902–1918 (2009).
40. B. A. Mazin et al., "A superconducting focal plane array for ultraviolet, optical, and near-infrared astrophysics," *Opt. Express* **20**, 1503 (2012).
41. F. Castelli and R. L. Kurucz, "New grids of ATLAS9 model atmospheres," 2004, https://www.google.co.in/url?sa=t&rct=j&q=&esrc=s&source=web&cd=2&ved=0CCgQFjABahUKEwjq6ZHHz6rHAhVTno4KHd2DAv0&url=http3A2F2Fwww.oact.inaf.it2Fcastelli2Fcastelli2Fgrids2Fpaper2Fpaper.ps&ei=yfHOVarhLNO8ugTdh4roDw&usg=AFQjCNHpHLD2SYtluD-Vkcyg3fnWgSHOqA&cad=rja (15 August 2015).
42. M. Kuchner, "ZODIPIC: Zodiacal Cloud Image Synthesis," *Astrophysics Source Code Library*, http://adsabs.harvard.edu/abs/2012ascl.soft02002K (2012).
43. G. Serabyn, "High contrast laboratory demonstrations with the vortex coronagraph," in *American Astronomical Society Meeting*, p. 113, American Astronomical Society (2014).

Timothy Cook specializes in developing novel instrumentation and data analysis techniques. He is currently working on instruments to study phenomena ranging from the formation of the structure of the universe to the atmospheres and environments of planets around nearby stars to the structure and carbon content of forests on Earth. His primary research thrust is the use of suborbital experiments to study astrophysical phenomenon.